Astronomy & Astrophysics manuscript no. kovarietal_finalpdf_20141031
November 10, 2014
©ESO 2014

Antisolar differential rotation of the K1-giant σ Geminorum revisited

Zs. Kővári[1], L. Kriskovics[1], A. Künstler[2], T. A. Carroll[2], K. G. Strassmeier[2], K. Vida[1], K. Oláh[1], J. Bartus[1], and M. Weber[2]

[1] Konkoly Observatory of the Hungarian Academy of Sciences, Konkoly Thege út 15-17., H-1121, Budapest, Hungary
e-mail: kovari@konkoly.hu
[2] Leibniz-Institute for Astrophysics (AIP), An der Sternwarte 16, D-14482 Potsdam, Germany

Received ; accepted

arXiv:1411.1774v1 [astro-ph.SR] 6 Nov 2014

ABSTRACT

Context. Surface differential rotation and other global surface flows on magnetically active stars are among the observable manifestations of the stellar dynamo working underneath. Therefore, such observations are important for stellar dynamo theory and useful constraints for solar dynamo studies as well.
Aims. The active K1-giant component of the long-period RS CVn-type binary system σ Gem and its global surface flow pattern is revisited.
Methods. We refine the differential rotation law from recovering the spot migration pattern. We apply a detailed cross-correlation technique to a unique set of 34 time-series Doppler images recovered using data from 1996/97. By increasing the number of the available cross-correlation function maps from the formerly used 4 to 17 we expect a more robust determination of the differential surface rotation law. In addition, we present a new time-series Doppler imaging study of σ Gem using our advanced surface reconstruction code *iMap* for a dataset collected in 2006/07.
Results. Results from the reprocessed cross-correlation study confirm that the star performs antisolar-type differential rotation with a surface shear α of -0.04 ± 0.01, i.e., almost a factor of two stronger compared to the previously claimed value. We also confirm the evidence of a global poleward spot migration with an average velocity of $0.21 \pm 0.03\,\mathrm{km\,s^{-1}}$, in accordance with theoretical predictions. From the new observations we obtain three subsequent Doppler images. The time evolution of these images confirms the antisolar-type differential rotation of the same amount.

Key words. stars: activity – stars: imaging – stars: late-type – stars: starspots – stars: individual: σ Gem

1. Introduction

Differential rotation (hereafter DR) on stars with convective envelopes carries important information on the dynamo process beneath the surface. The combined effects of the Coriolis force and stratification lead to a Reynolds stress and a horizontal component in the convective heat flux that result in a deviation from the cylinder-shaped velocity pattern and thus in DR (Kitchatinov & Rüdiger 1995, Käpylä et al. 2011, Warnecke et al. 2013). The rotation pattern predicted is predominantly solar-type, even for K giants, and the total surface shear varies strongly with the effective temperature and weakly with the rotation rate (Küker & Rüdiger 2011, 2012). However, anti-solar DR can be maintained by strong meridional circulation, as suggested by Kitchatinov & Rüdiger (2004). Theoretical support for the existence of antisolar-type DR in cool single stars was recently reinforced by Gastine et al. (2014) who found that stars with large Rossby numbers maintain the initial anti-solar pattern. Note though, that anti-solar DR was reported mostly for giants in close binary systems, where tidal forces could have a strong influence.

It is understood that in close binaries, such as the RS CVn-systems, tidal effects help maintain the fast rotation and thus higher levels of magnetic activity. Furthermore, tidal coupling between the star with a differentially rotating envelope and its companion star is thought to play a significant role (cf. Scharlemann 1981, 1982, Schrijver & Zwaan 1991, Holzwarth & Schüssler 2002, 2003). Retrieving the right connection between characteristic parameters of magnetic activity on binary stars and the exact physical parameters of the binary system will bring us closer to understanding activity in star-hot Jupiter systems as well.

Gaining deeper observational insight into magnetic dynamos in active stars and their comparison with that in the Sun produces important experimental input for dynamo theory. Still, it is not fully understood how stellar dynamos work. Therefore, theoretical development needs continuous feedback from observations on a sample of stars of different types.

We have learned from solar studies that sunspot groups tend to move together with the solar plasma, i.e., tracking sunspots can reveal DR and other surface flow fields like meridional circulation (e.g., Wöhl 2002, Wöhl et al. 2010). If time resolved surface maps are available for spotted stars, starspots are also suitable for tracking stellar surface velocity fields. Korhonen & Elstner (2011) found in their mean-field simulations that the large-scale dynamo field does not trace the differential rotation while the small-scale fields very well do. Time-series Doppler imaging is a powerful tomographic inversion technique to recover the time evolution of the surface patterns on spotted stars (Strassmeier & Bartus 2000, Marsden et al. 2007). Surface flows on stars have already been detected by analyzing such 'Doppler-

Send offprint requests to: Zs. Kővári, e-mail: kovari@konkoly.hu

movies' frame-by-frame (see, e.g., Kővári et al. 2004, 2007a, 2009).

In this work we revisit the rapidly-rotating K1-giant σ Geminorum (75 Gem, HR 2973, HD 62044) by performing a new time-series Doppler imaging analysis. σ Gem is a long-period ($P_{\rm rot}$ = 19.6 days) RS CVn-type system with a K1III primary star and an unseen companion star. A summary of its astrophysical parameters was given in Kővári et al. 2001 (hereafter Paper I). An exceptional possibility of collecting long-term data for such purposes was a 70-night long observing run with the 1.5m McMath-Pierce telescope at Kitt Peak National Solar Observatory in 1996/97. The data were used to prepare six time-series Doppler maps (see Paper I), which revealed cool spots at low to mid-latitudes, but none of the maps recovered a polar spot. Simultaneous photometric data showed a temporal evolution of the light curve during the full 3.6 rotation cycles. This was reconfirmed by a comparative analysis of the consecutive Doppler maps. However, in spite of this spot evolution, no conclusive DR pattern from a simple cross-correlation of consecutive maps was found, which was attributed to the masking effect of short-term spot changes. Those six time-series Doppler maps were re-analyzed by Kővári et al. (2007b, hereafter Paper II, but see also 2007c) using a more sophisticated cross-correlation technique, developed for time-series Doppler-maps. This more detailed analysis yielded anti-solar type differential rotation with a surface shear of $\alpha \approx -0.022$. Evidence of a poleward migration trend of spots was also found with an average velocity of $\approx 0.3\,{\rm km\,s^{-1}}$.

In Sect. 2 of this paper we present a new time-series of Doppler images including 34 frames, for two mapping lines, independently. This Doppler-movie is used to perform an even more detailed study (see Sect. 2.4) in order to confirm or confute our former findings. In Sect. 3 an additional Doppler surface image reconstruction is performed using a set of high-resolution spectra obtained with the 1.2m STELLA-I telescope (Tenerife, Spain) in 2006/07. In Sect. 4 the results from old and new data are compared with each other and discussed. The revealed DR law for σ Gem is set against other detections for RS CVn-type binaries in order to a better understanding how differential rotation could be affected by tidal forces in RS CVn-type close binaries.

2. Doppler images of σ Gem for 1996/97

2.1. The NSO time series

The data that enabled a new time-series Doppler-imaging analysis consist of 52 high-resolution optical spectra, taken at NSO/McMath during a 70 day-long observing run in 1996/97. The spectral range incuded two mapping lines, namely Fe I at 6430Å and Ca I at 6439Å that are used for the imaging process. From these 52 time-series spectra 34 data subsets are formed in such a way that every subset holds 18 consecutive spectra, i.e., the first subset consists of the first 18 observations, the second subset is formed from spectra of serial numbers between 2 and 19, and so on, while the last (34th) subset consists of the last 18 spectra. Subsets cover approximately one rotation period, thus are suitable for recovering altogether 34 'Doppler-frames' from them, simultaneously for the two mapping lines with our Doppler imaging code TempMap (Rice et al. 1989, Rice & Strassmeier 2000).

2.2. Is σ Gem elliptical?

It was demonstrated in Kővári et al. (2007a) that neglecting a possible ellipsoidal distortion, i.e., tidally induced Roche-geometry of the evolved component in a close binary system such as σ Gem, can introduce systematic errors into the Doppler reconstruction. Ellipsoidal variation of σ Gem might be indicated by the double wave that came forward from long-term photometric data from ≈13 years (see Fig.1), which, on the other hand, could also be explained by two preferred active longitudes where starspots or starspot groups tend to appear (Oláh et al. 1988). Since formerly (Papers I and II) spherical geometry was assumed for this target, at this point we switch to using TempMap$_\varepsilon$, a subversion of our inversion code developed specifically for imaging ellipsoidally distorted stars, in order to scan the significance of the possible ellipsoidal shape on the Doppler reconstruction (for the definition of the stellar distortion parameter ε and for the description of TempMap$_\varepsilon$ see Kővári et al. 2007a). The Doppler imaging procedure allows to fine-tune some stellar parameters by searching for the minimum of the goodness-of-fit of the Doppler reconstruction (Unruh 1996), therefore we fine-tuned ε over a reasonable range of the parameter space. The resulting O-C map suggested ignorable distortion (most likely $\varepsilon \approx 0$) , thus, we kept the spherical assumption, as concluded also by Duemmler et al. 1997.

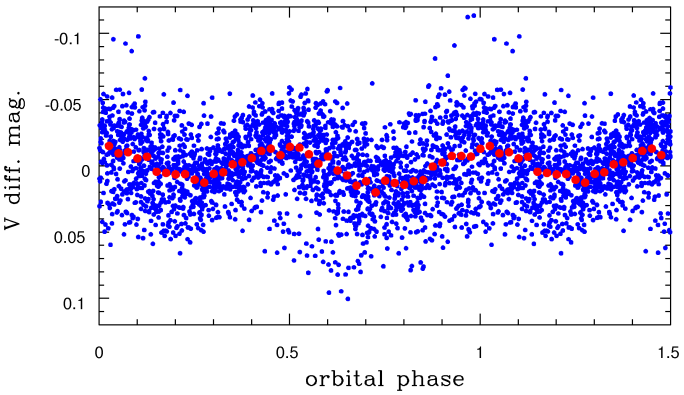

Fig. 1. Photometric V observations of σ Gem from ≈13 years are phased with the orbital period after removing long-term trends. The double wave can be caused by either ellipticity or starspots that appear stably at preferred active longitudes.

2.3. The Doppler-movies

The 34 finalized Doppler images for the combined (Fe I-6430 + Ca I-6439) line reconstructions in time order give the motion picture of the time-evolution of the stellar surface in the course of 3.6 consecutive stellar rotations. The respective maps for the two different mapping lines agree well, and confirm our former result that spots are found mostly at low to mid-latitudes, but no spots appear near the pole. As examples, Fig. 2 shows three surface maps from the entire set, namely the 1st, the 17th, and the last, i.e., 34th, corresponding to mid-HJDs of 2,450,400.41, 2,450,423.58 and 2,450,444.02, respectively, i.e., the three maps follow each other by approximately one rotation period.

2.4. Antisolar-type differential rotation

Surface differential rotation can be detected from cross-correlating in longitudinal direction the consecutive but contigu-

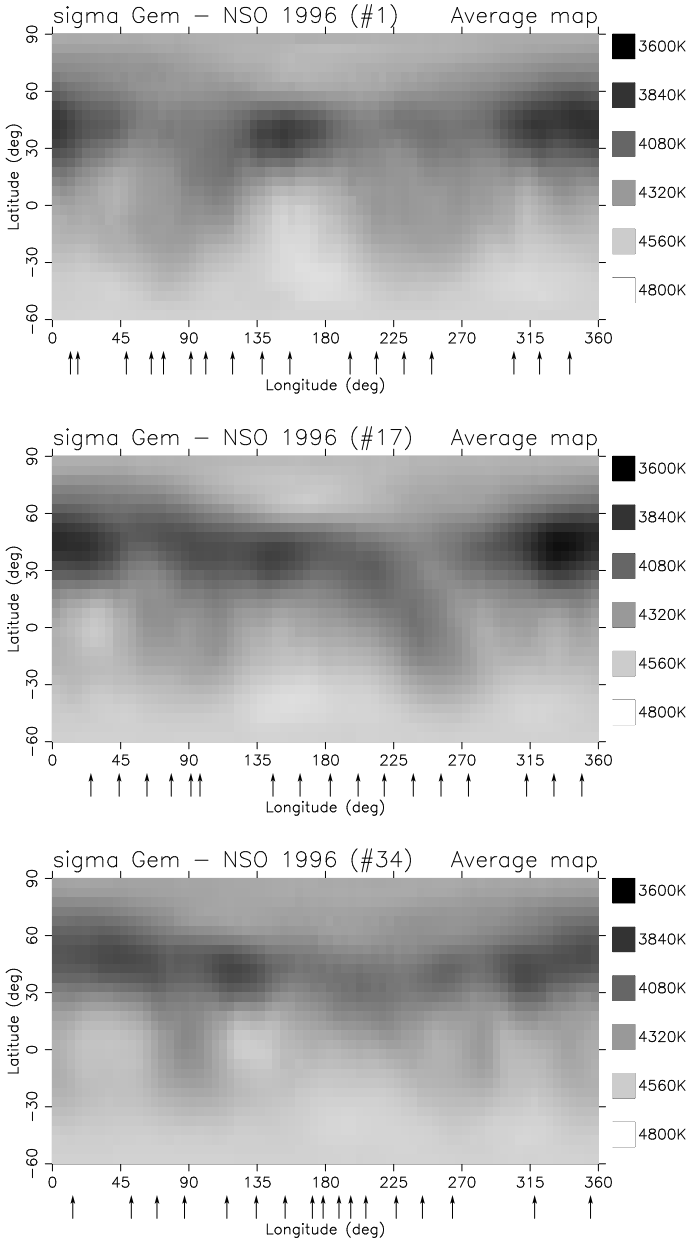

Fig. 2. Snapshots from the NSO time-series Doppler images of σ Gem. As examples, the 1st (top), the 17th (middle) and the last (bottom) combined (Fe+Ca) maps are shown. Arrows below the maps mark the phases of the observations. Time lags between the consecutive maps are 23.17 days (from 1st to 17th) and 20.44 days (from 17th to 34th).

ous Doppler image pairs, i.e., successive maps with the least possible time gaps. This way the blurring effect of the rapid spot evolution can be reduced, since the time lag is minimized. By averaging all the 17 available cross-correlation maps, the differential rotation pattern can be amplified. For this method, called ACCORD (acronym from average cross-correlation of Doppler-images) see e.g., Kővári et al. 2004, 2007a, Paper II, 2009, 2012). For further processing, the Fe I-6430 and Ca I-6439 image reconstructions were combined. The resulting average cross-correlation function (ccf) map is shown in Fig. 3. On the ccf map we fit the correlation peak for each latitudinal stripe of 5°-bin with a Gaussian profile. Gaussian peaks (with their FWHMs as error bars) are then fitted with a quadratic DR law of the form

$$\Omega(\beta) = \Omega_{\rm eq}(1 - \alpha \sin^2 \beta\,), \qquad (1)$$

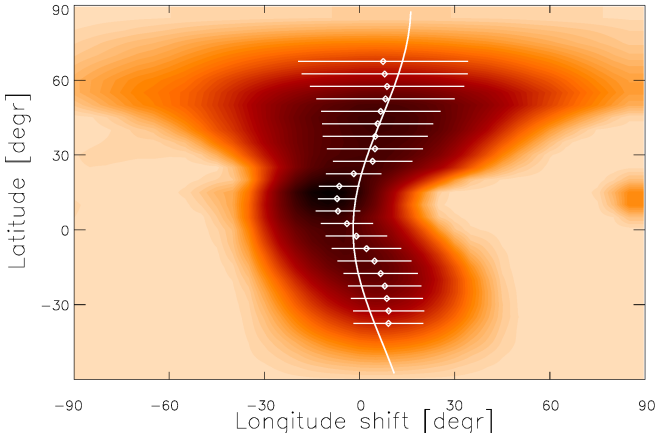

Fig. 3. Average cross-correlation function map of σ Gem from the NSO 1996/97 dataset. The resulting differential rotation pattern for the combined (Fe+Ca) time-series Doppler images gives evidence of anti-solar type differential rotation. The background shade scales the strength of the correlation (white: no correlation, dark: strong correlation). The dots are the correlation peaks per 5°-latitude bin. Their error bars are defined as the FWHMs of the corresponding Gaussians. Assuming a quadratic DR law the derived surface shear parameter α is –0.04±0.01.

where $\Omega(\beta)$ is the angular velocity at latitude β, while the surface shear parameter α is defined as $(\Omega_{\rm eq} - \Omega_{\rm pole})/\Omega_{\rm eq}$ where $\Omega_{\rm eq}$ and $\Omega_{\rm pole}$ are the angular velocities at the equator and at the pole, respectively. By applying this simple 2nd degree solar model we can estimate the order of the surface shear and determine whether the DR pattern is of solar or antisolar type, yet, without overrating the information content of the data. In practice we expect the DR curve to be more complicated, especially since tidal forces may induce non-axisymmetric structures in the DR pattern. The resulting correlation pattern in Fig. 3 indicates antisolar-type differential rotation, in agreement with Paper II. Indeed, the average correlation pattern became more significant, according to the standard deviations of the values in the average ccf map. The fitted parameters of the revised rotation law are $\Omega_{\rm eq} = 18.26 \pm 0.07$ [°/day] and $\alpha = -0.04 \pm 0.01$, with a lap time of ≈500 days, i.e., the redetermined surface shear is found to be almost two times stronger compared to the result in Paper II, where only 6 Doppler maps and so only 4 ccf maps were available. Nevertheless, this result is still in good agreement with the previous finding, considering the limitations from Doppler imaging and the cross-correlation method itself, as well as the estimated error bars.

2.5. Poleward drift of spots

Latitudinal shifts of spots can also be measured from the time-series Doppler images by applying the average cross-correlation technique along latitudinal columns, i.e., perpendicular to rotation (Weber & Strassmeier 2001; Kővári et al. 2007a; Paper II). First, we apply this method for the available Doppler image pairs (i.e., 17 latitudinal ccf maps). The averaged latitudinal ccf map (see Fig. 4) indicates a joint poleward spot migration, such like in Paper II, yielding ≈ 4° per rotation period. However, despite the conspicuous correlation pattern of a joint positive shift, the method of latitudinal cross-correlation suffers from an incompleteness due to the singularity rising towards the pole. To avoid this imperfection, we carried out another study, as follows.

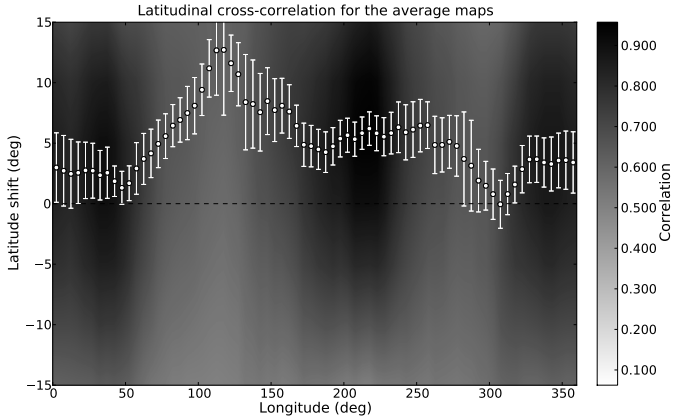

Fig. 4. Average latitudinal cross-correlation map from time-series Doppler images. 17 image pairs are averaged for the combined (Fe+Ca) reconstructions. Best correlating latitudinal shifts are marked with dots (Gaussian peaks), the corresponding error bars are proportional to the Gaussian FWHMs. The joint positive shift suggests poleward spot migration at an average velocity of $\approx 4^\circ$ per rotation period.

For a more reliable measure of the poleward drift (and for a better visualization as well) we cut our Mercator-maps longitudinally into 72 meridional slices of 5° width each. For a given longitude value l, the corresponding meridional stripe is normalized for the maximum temperature offset (i.e., the temperature minima) and finally these stripes are ranked in time order. Resulting plots (see examples in Fig. 5 top) indicate the meridional replacement of the temperature minima over the 34 time-series Doppler images for the given longitude l. Fig. 5 clearly suggests a poleward drift of the most prominent features. To quantify this drift we fitted the trace of the temperature minima by straight lines. The resulting fits with their mean (plotted in Fig. 5 bottom) estimate an average poleward flow of $2\overset{\circ}{.}3 \pm 0\overset{\circ}{.}3$ per rotation period (the error is the standard deviation of the weighted mean) This value is slightly smaller than the result from the average latitudinal cross-correlation study, but still in accordance with it (note, e.g., that the steepest slope from the top four panels in Fig. 5 corresponds to $l = 115^\circ$, which is just the longitude of the maximum latitude shift in Fig. 4). With the stellar parameters from Paper I, this velocity would correspond to 203 ± 27 m s^{-1} on the stellar surface.

3. Doppler images for 2006/2007

3.1. The STELLA time series

A spectroscopic dataset with altogether 71 observations were collected during ≈5 rotation cycles between 30th September 2006 and 7th January 2007 with the 1.2m STELLA-I telescope (Tenerife, Spain), equipped with STELLA Echelle Spectrograph (SES) (Weber et al. 2008, Strassmeier et al. 2010). All spectra covered the wavelength range from 390 nm - 880 nm. The resolving power was R = 55 000 corresponding to a spectral resolution of 0.12 Å at a wavelength of 650 nm. Further details of the performance of the system were reported by Weber et al. (2012) and Granzer et al. (2010).

Unfortunately, the dataset included a few large gaps which compromised the phase coverage, thus, a detailed time-series analysis, similar to the one described in Sect. 2 could not be possible. After some attempts, we formed three subsets, which came more or less evidently from the data distribution. However,

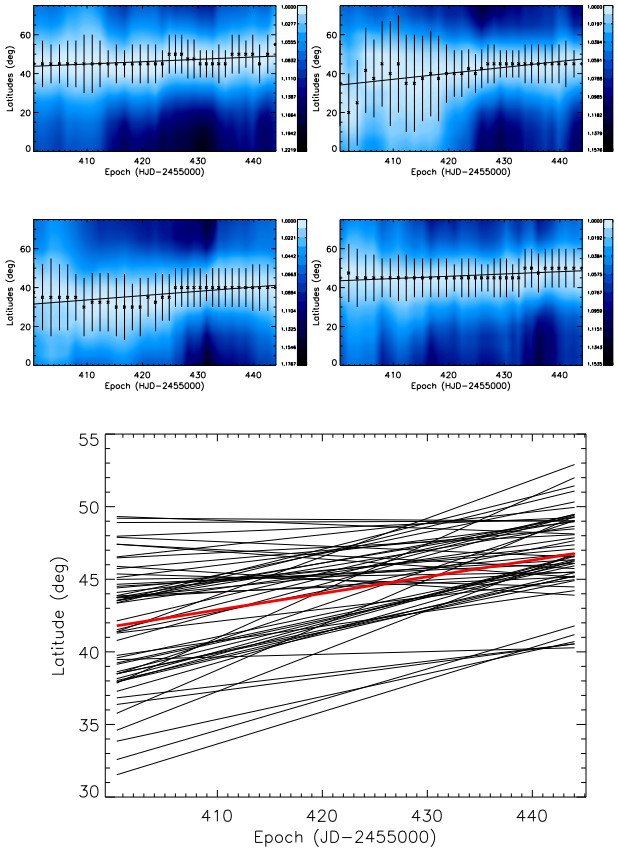

Fig. 5. Top: examples of meridional spot redistributions during the covered time span of about 43.5 days at arbitrarily chosen quadrant longitudes of 25°, 115°, 205° and 295° (top: left, right, below: left, right, respectively). In each case, the replacements of the maximum temperature offsets (dots) are fitted with a 1st degree function. Bottom: all the 72 available line fits. Red (thick) line indicates their average slope, suggesting a common poleward flow of $2\overset{\circ}{.}3$ per rotation period, consistently with the result shown in Fig. 4.

to further improve phase coverage, we tried to fill in the largest phase gaps, (involving only a few neighbouring observations), still, with keeping the data consistency. We note that such phase exchange had no significant impact on the reconstruction, thus, finally we kept the three subsets listed in Table 1, which have acceptable phase distributions, and are independent from each other, therefore suitable for cross-correlation study.

The observing log in Table 1 lists the HJDs with the corresponding observing dates and phases, and the signal-to-noise values for the three data subsets (S1, S2, S3). All spectras are phased using the same ephemeris as in Papers I-II:

$$HJD = 2,450,388.36853 + 19.60447 \times E. \quad (2)$$

3.2. The image reconstruction code iMap

Here we give a very brief description of the DI and ZDI code *iMap* we have used in this work (see Carroll et al. 2012 for further details). In its latest version the code performs a new multiline inversion to use the information of a large number of photospheric line profiles simultaneously. The line profiles are calculated by solving the full (polarized) radiative transfer (Carroll, Kopf & Strassmeier 2008). Individual atomic line parameters are taken from the VALD line database (Kupka et al. 1999). The

Table 1. Observing log of STELLA-I SES spectra from 2006/2007.

S1				S2				S3			
HJD	Date	Phase	S/N	HJD	Date	Phase	S/N	HJD	Date	Phase	S/N
(2454000+)	(yy-mm-dd)	([a])	([b])	(2454000+)	(yy-mm-dd)	([a])	([b])	(2454000+)	(yy-mm-dd)	([a])	([b])
008.666	06-09-30	0.667	172	029.617	06-10-21	0.736	72	069.542	06-11-30	0.772	187
008.711	06-09-30	0.669	223	029.732	06-10-21	0.742	119	069.589	06-11-30	0.775	200
009.659	06-10-01	0.718	168	030.610	06-10-22	0.786	131	069.632	06-11-30	0.777	183
009.707	06-10-01	0.720	224	030.665	06-10-22	0.789	133	071.595	06-12-02	0.877	203
011.659	06-10-03	0.820	198	030.726	06-10-22	0.792	119	071.637	06-12-02	0.879	196
011.704	06-10-03	0.822	185	049.565	06-11-10	0.753	210	071.778	06-12-02	0.886	234
012.657	06-10-04	0.871	138	050.554	06-11-11	0.804	207	092.664	06-12-23	0.952	108
012.701	06-10-04	0.873	160	053.563	06-11-14	0.957	80	095.493	06-12-25	0.096	121
012.745	06-10-04	0.875	149	056.686	06-11-17	0.116	186	095.746	06-12-26	0.109	156
013.739	06-10-05	0.926	109	060.588	06-11-21	0.315	56	096.441	06-12-26	0.144	133
015.652	06-10-07	0.023	186	062.536	06-11-23	0.415	237	096.688	06-12-27	0.157	140
015.700	06-10-07	0.026	184	062.581	06-11-23	0.417	229	097.473	06-12-27	0.197	82
018.640	06-10-10	0.176	193	062.626	06-11-23	0.419	240	100.430	06-12-30	0.348	214
018.696	06-10-10	0.179	172	062.668	06-11-23	0.422	228	101.424	06-12-31	0.398	177
021.629	06-10-13	0.328	179	063.525	06-11-24	0.465	176	104.415	07-01-03	0.551	211
021.694	06-10-13	0.331	105	063.576	06-11-24	0.468	218	105.467	07-01-04	0.605	127
022.627	06-10-14	0.379	143	063.621	06-11-24	0.470	218	105.523	07-01-05	0.607	225
022.688	06-10-14	0.382	153	074.500	06-12-04	0.025	216	105.564	07-01-05	0.610	116
022.733	06-10-14	0.384	174	074.592	06-12-05	0.030	208	106.427	07-01-05	0.654	160
044.583	06-11-05	0.499	197	074.634	06-12-05	0.032	176	107.454	07-01-06	0.706	270
044.690	06-11-05	0.504	211	074.770	06-12-05	0.039	181	107.519	07-01-07	0.709	89
				076.600	06-12-07	0.132	235				
				076.642	06-12-07	0.134	158				
				076.755	06-12-07	0.140	196				
				077.480	06-12-07	0.177	239				
				077.524	06-12-08	0.179	222				
				077.575	06-12-08	0.182	193				
				077.620	06-12-08	0.184	220				
				077.779	06-12-08	0.192	209				

Notes. [(a)] Phases are computed using Eq. 2. [(b)] Signal-to-noise (S/N) ratios correspond to the mean value for all extracted line profiles in the range of 5000–6500 Å.

code uses Kurucz model atmospheres (Castelli & Kurucz 2004) which are interpolated for each occurrent temperature, gravity and metallicity values through the inversion.

The typical ill-posed nature of the problem is tackled with an iterative regularization based on a Landweber algorithm (Carroll et al. 2012). This has the advantage that no additional constraints are imposed in the image domain. The surface segmentation for the current problem is set to a $5^\circ \times 5^\circ$ equal-degree partition. For each surface segment the full radiative transfer of all involved line profiles are calculated according to the current effective temperature and atmospheric model. The line profile discrepancy is reduced by adjusting the surface temperature of each segment according to the local (temperature) gradient information until the O-C minimum is reached.

3.3. Doppler image reconstructions

A big advantage of the inversion code *iMap* compared to the original TempMap code is the fact, that during the inversion process several (typically 20-30) spectral lines are taken into account simultaneously. This way the signal-to-noise ratio is increased by a factor of ≈5 which improves the resolving power of distortions in a line profile caused by surface spots. Furthermore, the surface reconstruction benefits from a large number of lines, as different absorption lines form in different photospheric depths. In the case of σ Gem 20 suitable absorption lines were chosen, including 16 Fe I and 4 Ca I lines in the range between 5000–6500Å. These lines were selected by their depth of formation, blends, continuum and temperature sensitivity. The two mapping lines often used for TempMap inversions, i.e., Fe I at 6430Å and Ca I at 6439Å are included as well. Astrophysical parameters were taken from Paper I.

Resulting Doppler images are plotted in Fig. 6. The corresponding line profile fits for the combined spectra are plotted in Fig. 7. All reconstructed spots are located between around 30° and 70° latitudes with a minimum spot temperature of ≈3800 K.

We note that the surface maps resemble those of the previous Doppler study in Paper I, i.e., having dominant cool regions at mid-latitudes and practically no polar spottedness. Concerning the short-term surface evolution, some redistribution of the spotted surface is clearly seen from one dataset to the next, despite the moderate time resolution of the maps.

3.4. Differential rotation

In analogy to our dataset from 1996/97, we derived the surface shear for the 2006/07 images with our cross-correlation technique ACCORD (cf. Sect. 2.4). Due to the disadvantageous phase coverage we could prepare only three data subsets for Doppler mapping, thus, only three cross-correlation function (CCF) maps were obtained for the three possible correlation pairs (i.e., S1-S2, S2-S3, and S1-S3).

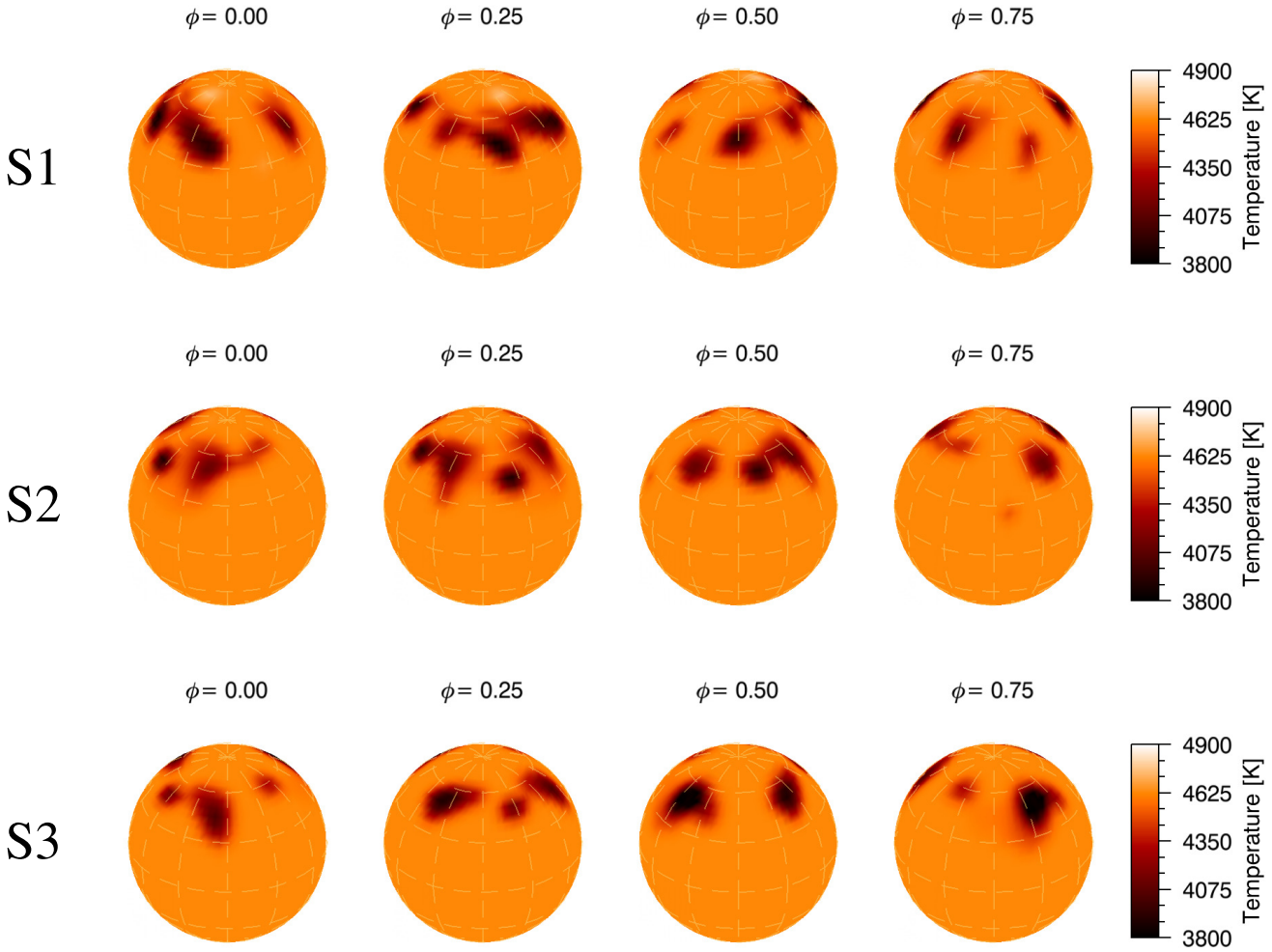

Fig. 6. Doppler images of σ Gem for three subsequent datasets S1, S2 and S3 (from top to bottom, respectively) in 2006/07. The corresponding mid-HJDs are 2,454,018.16, 2,454,061.38 and 2,454,092.50, respectively. Maps are shown in spherical projection in four quadrants with colorbars for the given temperature scale.

The average CCF map is shown in Fig. 8 and indicates antisolar-type DR with a surface shear of α = –0.04±0.01. The shear parameter derived for the 2006/2007 images is pretty much the same as the one presented in Sect. 2.4. We note, however, that due to the applied regularization we have limited information from a latitude belt below ≈30°, providing only six points in the CCF map to be fitted. The reliability of such a fit alone would be questionable. On the other hand, the antisolar kind and the order of the fitted rotation law is practically the same as reported for the NSO data before.

4. Discussion and conclusions

Antisolar-type differential rotation has been detected on a growing number of late-type giants (e.g., Strassmeier et al. 2003, Oláh et al. 2003; Weber et al. 2005; Vida et al. 2007; etc.). Theoretically, this kind of feature can be explained by including such terms like either large-scale surface inhomogeneities, or tidal effects in binaries, for maintaining enough strong meridional flow, which is essential (Kitchatinov & Rüdiger 2004). On the other hand, there are examples among RS CVn-type binaries that fulfil both criteria, yet perform solar type DR (increasing angular velocity towards the equator), e.g., ζ And (Kővári et al. 2007a, 2012), EI Eri (Kővári et al. 2009), V711 Tau (Petit et al. 2004), IL Hya (Kővári et al. 2014a), etc. It seems to be evident, that

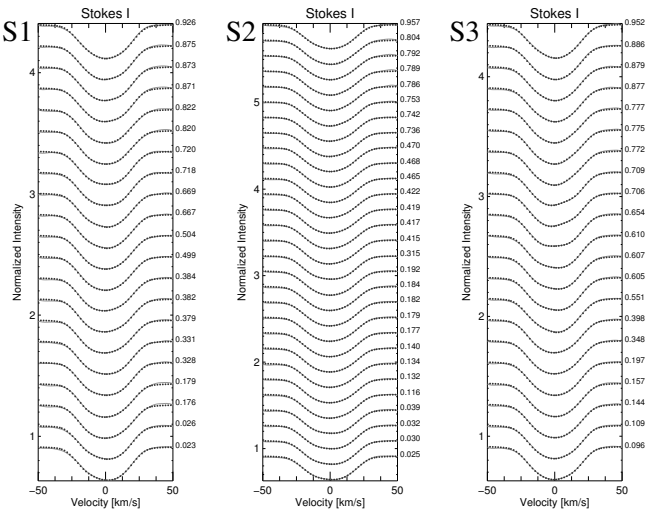

Fig. 7. Line profile fits of the three Doppler reconstructions in Fig 6.

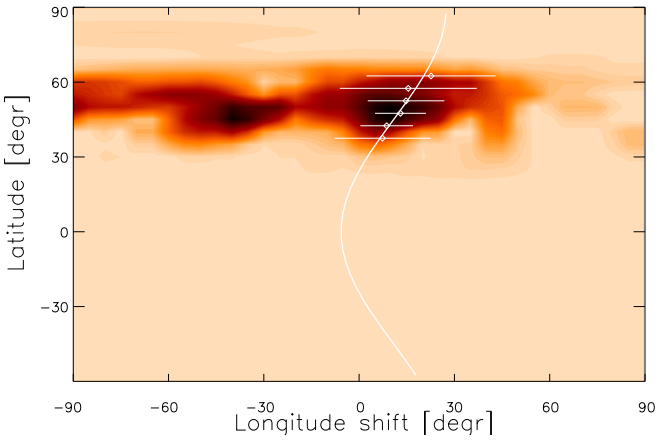

Fig. 8. Average cross-correlation function map of σ Gem from the STELLA 2006/2007 dataset. The background shade scales the strength of the correlation (white: no correlation, dark: strong correlation). The dots are the correlation peaks per 5°-latitude bin. Their error bars are defined as the FWHMs of the corresponding Gaussians. Assuming a quadratic DR law the derived surface shear parameter α is –0.04±0.01.

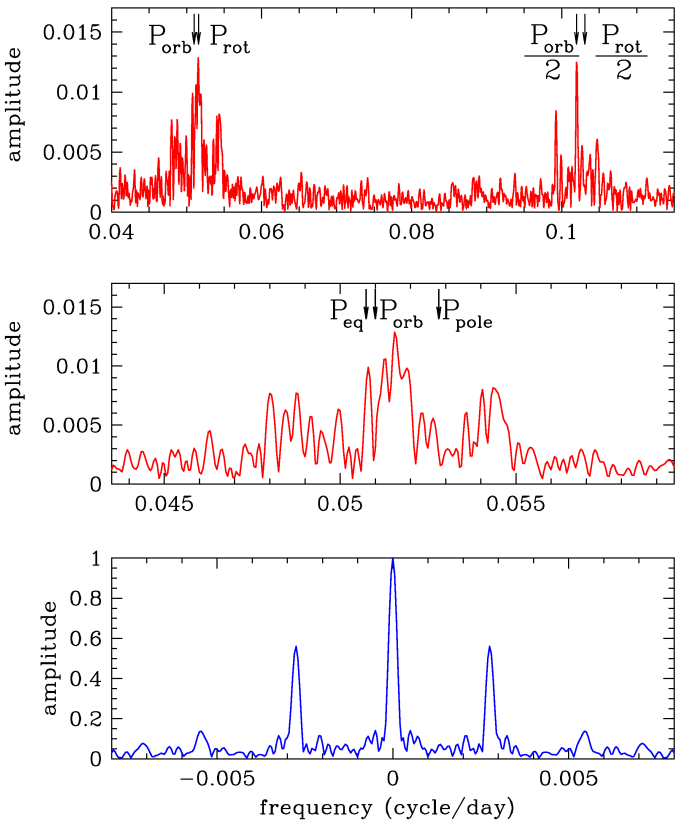

Fig. 9. The Fourier amplitude spectrum of σ Gem using V-band photometry of about 13 years. Top: power spectrum showing the strongest peak (P_{rot}) with the orbital period (P_{orb}) aside, and their overtones. Middle: amplitude spectrum around the orbital period with marking the equatorial and polar rotation periods (P_{eq}, P_{pole}) from the differential rotation law in Sect. 2.4. Bottom: window function of the signal.

the strength and even the orientation of the DR are influenced by the close companions, although, it is not clear how. In many cases peculiar spot distributions (quadrature positions, spots facing towards or away from the companion) i.e., spots fixed in the orbital frame indicate coupling magnetic fields between the binary components. It is not understood, however, what kind of general relationship exists in close binaries between the characteristics of the DR and other astrophysical parameters (cf., e.g., Dunstone et al. 2008; Holzwarth & Schüssler 2003, but see also Gastine et al. 2014).

According to the mechanism introduced by Scharlemann (1981, 1982), in an RS CVn-type binary, after the synchronization reaches its terminal phase due to tidal dissipation, the surface of the star with a convective envelope will have parts that rotate slower than the orbital period, while other parts will rotate faster. The two regions are separated by the so-called co-rotation latitude, which can be determined from stellar and system parameters, thus, they can be compared directly with observations. Applying Scharlemann's (1981, 1982) theory for σ Gem, this separator latitude is estimated to be around 22°, i.e., essentially the same that we derived from our time-series Doppler study. This could also be the sign that in σ Gem tidal coupling either is near to or has already reached its relaxed phase.

Unfortunately, Doppler imaging provides only a limited sample of stars to be mapped, due to the known restrictions (e.g., inclination angle being far from extremes, large enough rotational broadening, good quality homogeneous data providing sufficient phase coverage, etc.). On the other hand, long-term photometric observations exist for a much wider sample of spotted stars in binary systems (e.g., Strassmeier et al. 1997, 2011, Oláh & Strassmeier 2002, Oláh et al. 2009, 2009, Lindborg et al. 2013, etc.), that can also be used for investigating the role of binarity in the formation of magnetic activity. Fourier analysis for the available V-band observations of about 13 years is shown in Fig. 9. Usually the strongest period signal is expected from the largest and coolest spots. According to the available time-series Doppler maps, during the covered time interval the coolest regions appeared mostly between ≈30-70° latitudes. This is quite in agreement with the results of the first Doppler imaging study of σ Gem (Hatzes 1993), as well as with our finding in Fig. 9, where the location of the strongest amplitude peak corresponds to some mid-latitude belt that is rotating faster than the orbit (cf. that the co-rotation latitude is at ≈22°). Indeed, this feature seems to be stable for much longer term than the range of our Doppler observations, affirming that tidal effects may organize preferred longitudes, as well as latitudes of activity in close binaries (cf. Kajatkari et al. 2014 and see also the summary by Oláh 2007).

We conclude, that, from our cross-correlation technique `ACCORD` for 34 time-series Doppler images of the active K1-giant σ Gem a clear sign of antisolar-type surface DR was derived with a shear of –0.04±0.01 and a lap time of ≈490 days. This result is almost a factor of two stronger than reported in Paper II, where only 6 time-series Doppler images were available. We note that artefacts related to imperfect Doppler reconstruction (e.g., due to sparse phase coverage or mirroring of a high latitude feature, etc.) have no significant impact on the retrieved DR pattern, when using `ACCORD` (see Kővári et al. 2014b and Appendix A). Furthermore, three additional Doppler surface reconstructions from a more recent dataset (see Sect. 3) enabled to arrive at a similar result, despite the unfavourable time resolution compared to the NSO 1996/97 data.

Reprocessing also the *latitudinal* cross-correlation study for the 34 time-series Doppler images resulted in a common poleward meridional migration of the spots. This detection, if attributed to the surface pattern of meridional circulation, would mean an average poleward velocity field of 203±27 m s^{-1}, supporting theoretical expectations (cf. Kitchatinov & Rüdiger

2004). Recently, Cole et al. (2014) reinforced the findings from mean-field theory that there is a non-axisymmetric dynamo mode in convective shell dynamos. Their direct 3-D numerical simulations even showed a retrograde mode (wave). It does not reflect the speed of the DR at any depth and could be an alternative explanation for the latitude drift of spots and even compete against or amplify the DR pattern.

Acknowledgements. Authors appreciate the referee's comments which helped to improve the paper. Authors from Konkoly Observatory are grateful to the Hungarian Scientific Research Fund (OTKA) for support through grant no. K-109276. This work is supported by the "Lendület-2009" and "Lendület-2012" Young Researchers' Program of the Hungarian Academy of Sciences. The authors acknowledge the support of the German *Deutsche Forschungsgemeinschaft, DFG* through projects KO 2320/1 and STR645/1. KGS acknowledges the generous allotment of telescope time at NSO.

References

Carroll, T. A., Kopf, M., & Strassmeier, K. G. 2008, A&A, 488, 781
Carroll, T. A., Strassmeier, K. G., Rice, J. B., & Künstler, A. 2012, A&A, 548, A95
Castelli, F., & Kurucz, R. L. 2004, arXiv:astro-ph/0405087
Cole, E., Käpylä, P. J., Mantere, M. J., & Brandenburg, A. 2014, ApJ 780, L22
Duemmler, R., Ilyin, I. V., & Tuominen, I. 1997, A&AS, 123, 209
Dunstone, N. J., Hussain, G. A. J., Collier Cameron, A., et al. 2008, MNRAS, 387, 1525
Gastine, T., Yadav, R. K., Morin, J., Reiners, A., & Wicht, J. 2014, MNRAS, 438, L76
Granzer, T., Weber, M., & Strassmeier, K. G. 2010, Advances in Astronomy, article id. 980182
Hatzes, A. 1993, ApJ, 410, 777
Holzwarth, V., & Schüssler, M. 2002, AN, 323, 399
Holzwarth, V., & Schüssler, M. 2003, A&A, 405, 291
Kajatkari, P., Hackman, T., Jetsu, L., Lehtinen, J. & Henry, G. W. 2014, A&A, 562, A107
Käpylä, P. J., Mantere, M. J., Guerrero, G., Brandenburg, A., & Chatterjee, P. 2011, A&A, 531, A162
Kitchatinov, L.L., & Rüdiger, G. 1995, A&A, 299, 446
Kitchatinov, L.L., & Rüdiger, G. 2004, AN, 325, 496
Korhonen, H., & Elstner, D. 2011, A&A, 532, 106
Kővári, Zs., Strassmeier, K. G., Bartus, J., et al. 2001, A&A, 373, 199
Kővári, Zs., Strassmeier, K. G., Granzer, T., et al. 2004, A&A, 417, 1047
Kővári, Zs., Bartus, J., Strassmeier, K. G., et al. 2007a, A&A, 463, 1071
Kővári, Zs., Bartus, J., Strassmeier, K. G., et al. 2007b, A&A, 474, 165
Kővári, Zs., Bartus, J., Svanda, M., et al. 2007c, AN, 328, No. 10, 1081
Kővári, Zs., A. Washuettl, A., Foing, B.H., et al. 2009, in: 15th Cambridge Workshop on Cool Stars, Stellar Systems and the Sun, 21-25 July, 2008, St Andrews, Scotland, Edited by E. Stempels, AIP Conf. Proc. Vol. 1094, p. 676
Kővári, Zs., Korhonen, H., Kriskovics, L., et al. 2012, A&A, 539, A50
Kővári, Zs., Kriskovics, L., Oláh, K., et al. 2014a, in: Magnetic Fields Throughout the Stellar Evolution, Proceedings of IAU Symposium 302, 26-30 August, 2013, Biarritz, France, Edited by M. Jardine, P. Petit & H. Spruit, Cambridge: Cambridge University Press, p. 379
Kővári, Zs., Bartus, J., Kriskovics, L., Vida, K., & Oláh, K., 2014b, in: Magnetic Fields Throughout the Stellar Evolution, Proceedings of IAU Symposium 302, 26-30 August, 2013, Biarritz, France, Edited by M. Jardine, P. Petit & H. Spruit, Cambridge: Cambridge University Press, p. 198
Küker, M., & Rüdiger, G. 2011, AN, 332, 933
Küker, M., & Rüdiger, G. 2012, AN, 333, 1028
Kupka, F., Piskunov, N., Ryabchikova, T. A., Stempels, H. C., & Weiss, W. W. 1999, A&AS, 138, 119
Lindborg, M., Mantere, M. J., Olspert, N., et al. 2013, A&A, 559, 97
Oláh, K., Panov, K.P., Pettersen, B.R., Valtaoja, E., & Valtaoja, L. 1988, A&A, 218, 192
Oláh, K., & Strassmeier, K. G. 2002, AN, 323, 361
Oláh, K., Jurcsik, J., & Strassmeier, K. G. 2003, A&A, 410, 685
Oláh, K. 2007, in: Binary Stars as Critical Tools & Tests in Contemporary Astrophysics, Proceedings of IAU Symposium 240, 22-25 August, 2006, Prague, Czech Republic, Edited by W.I. Hartkopf, E.F. Guinan & P. Harmanec, Cambridge: Cambridge University Press, p. 442
Oláh, K., Jurcsik, J., & Strassmeier, K. G. 2003, A&A, 410, 685
Oláh, K., Moór, A., Strassmeier, K. G., Borkovits, T., & Granzer, T. 2013, AN, 334, 625
Marsden, S. C., Berdyugina, S. V., Donati, J.-F., Eaton, J. A., & Williamson, M. H. 2007, AN, 328, 1047
Petit, P., Donati, J.-F., Wade, G. A., et al. 2004, MNRAS, 348, 1175
Rice, J. B., Wehlau, W. H., & Khokhlova, V. L. 1989, A&A, 208, 179
Rice, J. B., & Strassmeier, K. G. 2000, A&AS, 147, 151
Scharlemann, E. T. 1981, ApJ, 246, 292
Scharlemann, E. T. 1982, ApJ, 253, 298
Schrijver, C. J., & Zwaan, C. 1991, A&A, 251, 183
Strassmeier, K. G., Boyd, L. J., Epand, D. H., & Granzer, T. 1997, PASP, 109, 697
Strassmeier, K. G., & Bartus, J. 2000, A&A, 354, 537
Strassmeier K. G., Kratzwald L., & Weber M., 2003, A&A, 408, 1103
Strassmeier, K. G., Granzer, T., Weber, M., et al. 2010, Advances in Astronomy, 2010, article id. 970306
Strassmeier, K. G., Carroll, T. A., Weber, M., et al. 2011, A&A, 535, 98
Unruh, Y. C. 1996, in Stellar Surface Structure, ed. K. G. Strassmeier & J. L. Linsky, IAU Symp., 176, 35
Vida, K., Kővári, Zs., Švanda, M., et al. 2007, AN, 328, 1078
Weber, M., & Strassmeier, K. G. 1998, A&A, 330, 1029
Weber, M., & Strassmeier, K. G. 2001, A&A, 373, 974
Weber, M., Strassmeier, K. G., & Washuettl, A. 2005, AN, 326, 287
Weber, M. Granzer, T., & Strassmeier, K. G. 2012, Proc. SPIE, 8451
Weber, M., Granzer, T., Strassmeier, K. G., & Woche, M. 2008, Proc. SPIE, 7019,
Warnecke, J., Käpylä, P. J., Mantere, M. J., & Brandenburg, A. 2013, ApJ, 778, 141
Wöhl, H. 2002, AN, 323, 329
Wöhl, H., Brajša, R., Hanslmeier, A., & Gissot, S. F. 2010, A&A, 520, A29

Appendix A: Testing the effect of imperfect Doppler reconstruction on the DR pattern retrieved by ACCORD

Doppler reconstruction is often biased by imperfections. It is understood that either sparse phase coverage or low signal-to-noise ratio (S/N) can result in artificial shadows of dominant high latitude features. Such shadows and appendages at lower latitudes can be interfering when retrieving the latitudinal rotation law through spot tracking. We demonstrate that in our tests artefacts related to imperfect Doppler reconstruction due to low S/N and sparse phase coverage have no significant impact on the retrieved DR pattern, when using our average cross-correlation method called ACCORD. Details of the test can be found in Kővári et al. (2014b).

In Fig. A.1 top two original test images are seen which were arbitrarily chosen as examples from a series of 28 artificial surface temperature maps. These maps were prepared as time-series snapshots of a differentially rotating test star. A weak solar-type surface DR law was incorporated with $\alpha = 0.006$ shear parameter. Below the originals are the recoveries with different S/N values and phase coverages. It is clear that imperfections emanate from sparse phase coverage, even when no data noise is assumed (note that 8 spectra were taken for each map only). Low latitude shadows and such kind of imperfections become stronger when S/N decreases. Still, the respectively retrieved correlation patterns and their fits (see the right-hand panels of Fig. A.1) imply that such artefacts have no significant impact on either the sign or the magnitude of the resulting surface shear. We note, that in the test case the phase coverages were more unfavourable, S/N values were lower and the surface shear was much weaker compared to the case of σ Gem in Sect. 2 of this paper.

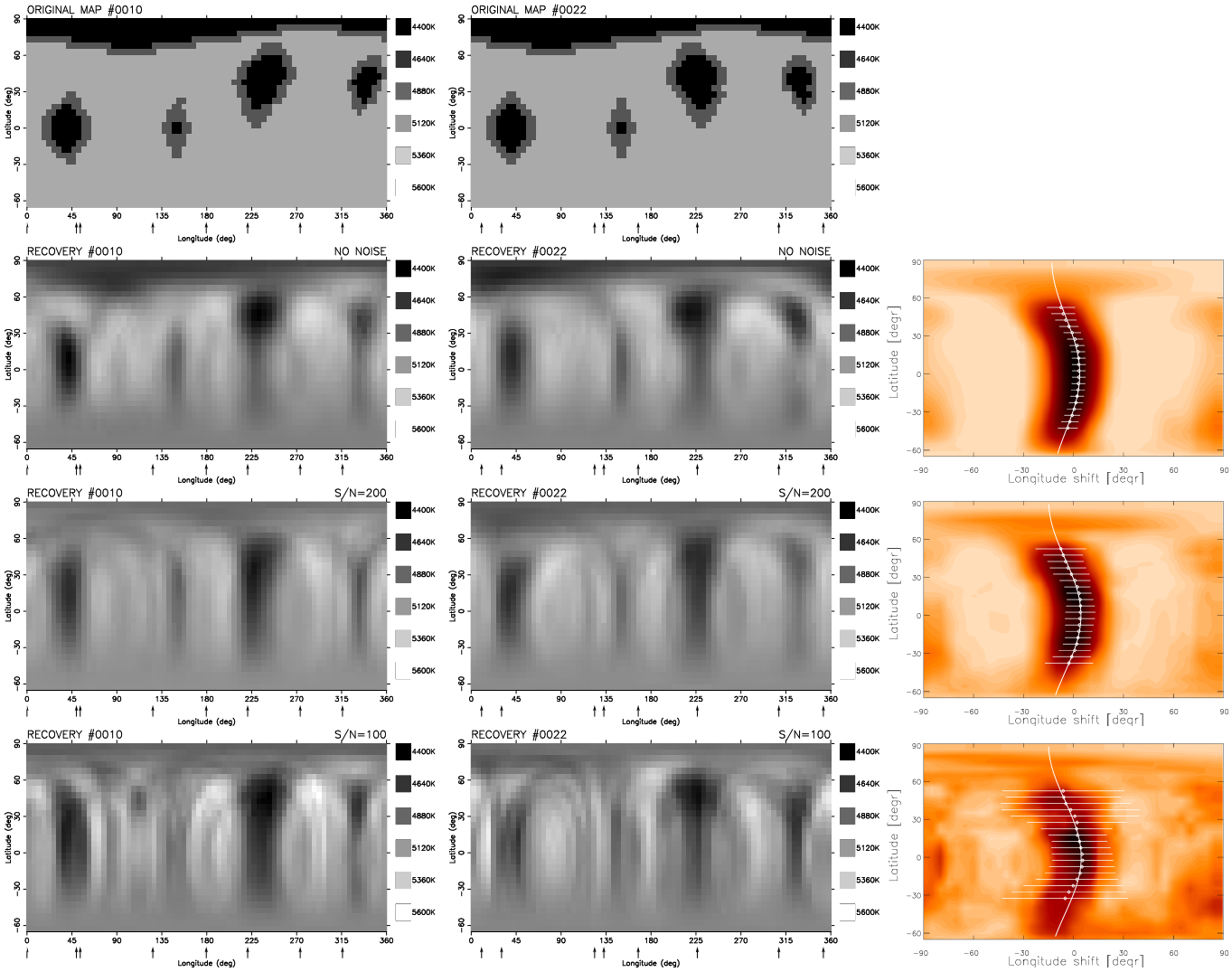

Fig. A.1. Top: two examples from a time series of 28 artificial surface temperature maps as snapshots of a differentially rotating test star applying $\alpha = 0.006$ surface shear. Below, in the second, third, and forth rows plotted are the corresponding recoveries with assuming no data noise, S/N=200, and S/N=100, respectively. Phases of the artificial observations are indicated by arrows underneath. In the right-hand column the retrieved DR functions are plotted as best fits (continuous lines) for the correlation patterns of the average cross-correlation function maps. The respective shear parameters are $\alpha = 0.0058 \pm 0.0002$ (no noise, right top), $\alpha = 0.0067 \pm 0.0006$ (S/N=200, right middle), $\alpha = 0.0069 \pm 0.0012$ (S/N=100, right bottom).